Check for updates

Bearing behavior of high-performance concrete-filled high-strength steel tube composite columns subjected to eccentrical load

Liangqin Jiang[1], Weichen Wang[1], Jing Ji[1,2]*, Hongguo Ren[3]*, Qingqin Wang[4], Ruohan Sun[3]*, Chenyu Yu[1], Huiling Zhang[1] and Gan Luo[1]

[1]Heilongjiang Key Laboratory of Disaster Prevention, Mitigation and Protection Engineering, Northeast Petroleum University, Daqing, China, [2]Key Laboratory of Earthquake Engineering and Engineering Vibration, Institute of Engineering Mechanics, China Earthquake Administration, Harbin, China, [3]Handan Key Laboratory of Building Physical Environment and Regional Building Protection Technology, School of Architecture and Art, Hebei University of Engineering, Handan, China, [4]China Academy of Building Research Co., Ltd., Beijing, China

In order to study the bearing capacity of high-performance concrete-filled high-strength steel tube (HCHST) composite stub columns subjected to eccentrical load, 22 HCHST composite stub columns, 4 concrete-filled steel tube (CFST) composite stub columns and 8 high-performance concrete-filled steel tube (HCST) composite stub columns were designed with the cubic compressive strength of concrete (f_{cu}), the yield strength of steel tube (f_y), the thickness of tube wall (t), the eccentricity (e) and slenderness ratio (λ) as the main parameters. Considering the nonlinear constitutive model of concrete and simplified constitutive model of steel, the finite element (FE) model of HCHST composite stub columns was established by ABAQUS software. By comparison with the existing test results, the rationality of the constitutive model and boundary conditions was verified. The variation of ultimate bearing capacity and the typical failure modes of HCHST composite stub columns under different parameters was analyzed. The results show that the specimens exhibit obvious bulge outward at the end of the steel tube and shear failure at the end of concrete. High-performance concrete (HPC) can significantly improve the ultimate eccentrical compression bearing capacity of composite columns, and high-strength steel tubes have better restraint effect on HPC. With the increasing of t, the ultimate eccentrical compression bearing capacity and the load-holding capacity of HCHST columns increases gradually, while the ultimate eccentrical compression bearing capacity decreases gradually with the increasing of λ and e. By introducing the reduction coefficient of eccentricity (φ_1) and the reduction coefficient of slenderness ratio (φ_2), the calculation formula of the eccentric bearing capacity of HCHST columns is proposed by statistical regression, which can lay a foundation for the application of HCHST columns in practical engineering.

Introduction

Concrete-filled steel tube (CFST) composite columns have been widely used in various building structures for their high bearing capacity, excellent plasticity and seismic performance (Wang et al., 2019; Ji et al., 2021a; Ji et al., 2021b). With the development of concrete materials (Cai et al., 2021; Ji et al., 2021c; Ding et al., 2021), high-performance concrete (HPC) (Yoo et al., 2012) has been commonly used in engineering for its self-compactness, high strength, high permeability and long service life (Huang et al., 2009; Sung et al., 2012; Wang and Liang, 2012; Yoon and Jang, 2015). The combination of HPC and high-strength steel tube (HST) has become a new trend in the development of composite structures (Yang et al., 2009). HPC-filled HST (HCHST) composite columns can not only bring into play the advantages of high strength and self-compacting of HPC, but also improve significantly the ultimate bearing capacity and the ductility of the composite columns.

A large number of studies were carried out on mechanical properties of HPC-filled steel tube (HCST) composite columns (Han and Yao, 2004; Guler et al., 2013; Ho et al., 2013; Ekmekyapar and Alhatmey, 2019). Static tests on 10 HCST composite stub columns under axial load were carried out by Gu et al. (1991), and the working mechanism and damage pattern of this kind of composite short columns were obtained, finally the calculation formula of axial bearing capacity of HCST composite short columns was proposed. Yu et al. (2002) carried out tests on 28 short columns of HCST composite stub columns under axial load, and the formulae for calculating the stress-strain curves of HCST composite short columns under axial load were proposed based on the experimental data. Tests on 8 ordinary CFST composite columns and 20 HCST composite columns subjected to axial and eccentrical loads were carried out by Yu et al. (2007), and the results showed that the main failure mode of HCST composite stub columns was the shear failure of concrete, and the ultimate bearing capacity formulae of HCST composite columns under axial and eccentrical loads given in the codes AISC, EC4 and DBJ13-51-2003 were reasonable. In 2010, tests on 18 steel reinforced self-compacting HPC-filled square steel tube composite columns under axial load were carried out by Zhu et al. (2010), and the variation regularity of the ultimate bearing capacity of this kind of composite columns with different parameters was obtained, and the calculation formula of the axial bearing capacity of composite columns was proposed based on the test data. In 2016, tests of 8 high-strength concrete-filled high-strength square steel tube composite columns under bending load were carried out by Li et al. (2019), and the results showed that the ultimate bearing capacity of composite columns under pure bending load increased gradually with the increasing of steel ratio and yield strength of steel tube, and the ultimate bearing capacity of composite columns obtained by finite element (FE) analysis

was in good agreement with the calculations of EC4. In 2020, Tests and FE analysis on ultra-HPC-filled round high-strength steel tube composite stub columns subjected to axial load were conducted by Wei et al. (2019),and the results showed that high-strength steel tubes provided more effective restraint for ultra-HPC, so high-strength steel tube was a better match with ultra-HPC. In 2021, FE analysis on the bearing capacity of hollow GFRP pipe-concrete-steel tube composite long columns subjected to eccentrical load was carried out by Ji et al. (2021d), and the results showed that with the increasing of thickness of GFRP tube, steel tube, and cubic compressive strength of concrete, the ultimate eccentric compression bearing capacity increased gradually, finally a formula for the bearing capacity of such composite columns under eccentric load was proposed by statistical regression.

So far, the research on HPC-filled high-strength steel tube (HCHST) composite stub columns have mainly focused on the axial compression bearing capacity, however, there are few studies on bearing capacity of the composite columns subjected to eccentrical load, therefore, it is essential to carry out the research on the mechanical performance of HCHST composite columns subjected to eccentrical load. Based on the nonlinear constitutive model of concrete and simplified constitutive model of steel, the mechanical behavior of HCHST composite columns with different parameters is analyzed by ABAQUS software. The formula on bearing capacity of this kind of composite columns subjected to eccentrical load is proposed by statistical regression.

Specimens design

To study the mechanical behavior of HCHST composite stub columns subjected to eccentrical load, 22 HPC-filled high-strength steel tube (HCHST) composite stub columns, four CFST composite stub columns and eight HCST stub columns are designed with the cubic compressive strength of concrete (f_{cu}), the yield strength of steel tube (f_y), the wall thickness of steel tube (t), the eccentricity (e) and the slenderness ratio (λ) as the main parameters. The schematic diagram and specific parameters of the specimens are shown in Figure 1; Table 1. λ is equal to L/D in Table 1.

Finite element model

Constitutive model for materials

Steel

The simplified double-broken line model is adopted as the constitutive model (CM) for steel, and 2.06×10^5 MPa and 0.3 are taken as the elastic modulus and the Poisson's ratio of steel, respectively.
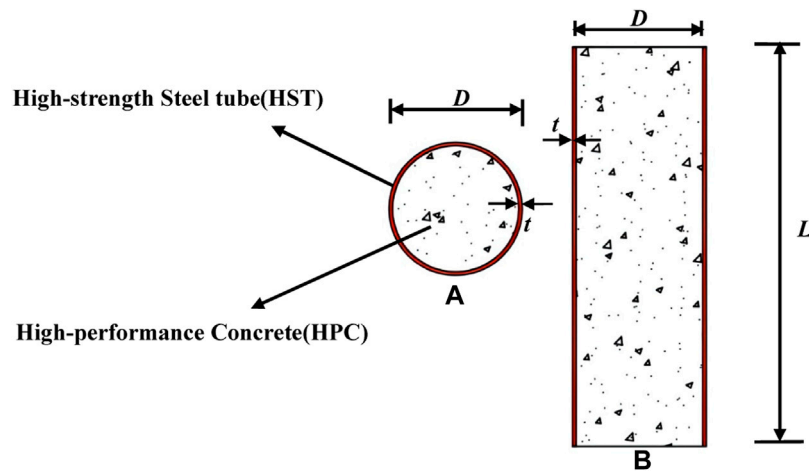
FIGURE 1
The schematic diagram and physical meaning of variables for specimens. **(A)** Cross section; **(B)** Longitudinal section.

Concrete

The constitutive models of concrete have been given by Han (2007), Mander et al. (1988), Teng et al. (2006), Ghorbi et al. (2013), Tao et al. (2013), Pagoulatou et al. (2014) and Qian et al. (2002) respectively, and the comparison of different constitutive models is shown in Figure 2. Yu et al. (2009) have confirmed that the constitutive model of concrete proposed by Han (2007). is applicable to high-performance concrete without fiber reinforcement, so the constitutive model of confined concrete proposed by Han (2007) is adopted here. Plastic damage model of concrete is selected accordingly during finite element modeling of ABAQUS.

The stress-strain relationship of concrete under uniaxial compression:

$$y = \begin{cases} 2x - x^2 & (x \le 1) \\ \dfrac{x}{\beta_0 (x-1)^{\left(1.6+\frac{1.5}{x}\right)} + x} & (x > 1) \end{cases} \quad (1)$$

Where $x = \varepsilon/\varepsilon_0$, $y = \sigma/\sigma_0$, $\sigma_0 = f_c$, $\varepsilon_0 = (1300 + 12.5 f_c) \times 10^{-6} + 800\xi^{0.2} \times 10^{-6}$.

The stress-strain relationship of concrete under uniaxial tension:

$$y = \begin{cases} 1.2x - 0.2x^6 & (x \le 1) \\ \dfrac{x}{0.31\sigma_p^2 \cdot (x-1)^{1.7} + x} & (x > 1) \end{cases} \quad (2)$$

Where $x = \varepsilon_c/\varepsilon_p$, $y = \sigma_c/\sigma_p$, $\sigma_p = 0.26 \times (1.25 f_c)^{2/3}$, $\varepsilon_p = 43.1\sigma_p$, and other variables can be found in the reference Han (2007). The elastic modulus of concrete is $4700 \times (f_c)^{0.5}$ Mpa according to ACI Committee 318 of the American Concrete Association (American Concrete Institute, 2005), where f_c is the cylindrical compressive strength of concrete.

Modeling process and boundary conditions

The FE models of 34 specimens were established by ABAQUS software as shown in Figure 3. The eight-joint hexahedral element type (C3D8R) were adopted to simulate the steel tube and concrete. The nonlinear symmetrical contact between steel tube and concrete was simplified as normal hard contact and tangential friction contact, and the Coulomb friction coefficient (μ) was set as 0.6. Two reference points were set near the upper and lower surfaces of the columns, namely RP1 and RP2. The reference points were, respectively, coupled with the top end and the bottom end of the columns. The displacements (U_x, U_y, UR_x, UR_z) of the top end for columns were constrained by RP1, and the displacements $(U_x, U_y, U_z, UR_x, UR_z)$ of the bottom end for columns were constrained accordingly by RP2.

Experimental verification of finite element models

In order to verify the rationality of the FE models, nine groups of HPC-filled steel tube composite stub columns subjected to axial load (Wang et al., 2013) and seven groups of CFST composite columns subjected to eccentrical load (Lee et al., 2019; Yu et al., 2007; Han 2007) were selected. The specific parameters of all

TABLE 1 Specific parameters of 22 HCHST composite columns, 4 CFST composite columns and 8 HCST composite columns.

Specimens	D/mm	L/mm	t/mm	f_{cu}/MPa	f_y/MPa	e/mm	λ
CFST-1	200	600	6	40	400	50	3
CFST-2	200	600	6	60	400	50	3
CFST-3	200	600	6	40	400	30	3
CFST-4	200	600	6	60	400	30	3
HCST-1	200	600	6	80	400	50	3
HCST-2	200	600	6	100	400	50	3
HCST-3	200	600	6	80	400	30	3
HCST-4	200	600	6	100	400	30	3
HCST-5	200	600	6	100	335	50	3
HCST-6	200	600	6	100	500	50	3
HCST-7	200	600	6	100	335	30	3
HCST-8	200	600	6	100	500	30	3
HCHST-1	200	600	6	100	700	50	3
HCHST-2	200	600	6	100	700	30	3
HCHST-3	200	600	2	100	700	50	3
HCHST-4	200	600	4	100	700	50	3
HCHST-5	200	600	8	100	700	50	3
HCHST-6	200	600	10	100	700	50	3
HCHST-7	200	600	2	100	700	30	3
HCHST-8	200	600	4	100	700	30	3
HCHST-9	200	600	8	100	700	30	3
HCHST-10	200	600	10	100	700	30	3
HCHST-11	200	600	10	100	700	40	3
HCHST-12	200	600	10	100	700	60	3
HCHST-13	200	600	10	100	700	70	3
HCHST-14	200	600	10	100	700	80	3
HCHST-15	200	600	4	100	700	40	3
HCHST-16	200	600	4	100	700	60	3
HCHST-17	200	600	4	100	700	70	3
HCHST-18	200	600	4	100	700	80	3
HCHST-19	200	400	10	100	700	50	2
HCHST-20	200	500	10	100	700	50	2.5
HCHST-21	200	400	10	100	700	30	2
HCHST-22	200	500	10	100	700	30	2.5

specimens were shown in Table 2. FE simulation analysis on 16 existing test specimens was carried out based on above FE modeling method, and the vertical load (N)-displacement (Δ) curves and mid-span load (N)-deflection (μ_m) curves of composite columns were obtained as shown in Figure 4. By comparing with the test curves, it could be seen from Figure 4 that the FE simulation curves were basically consistent with the test curves. The comparison between the simulated bearing capacity (N_a) and the experimental bearing capacity (N_t) was shown in Table 2 and Figure 5, and we could see that the maximum error was 9.4%, which could meet the requirements of engineering accuracy, so it was feasible to simulate the eccentrical compression behavior of

HCHST composite columns based on the proposed FE modeling method.

Parameter analysis

FE analysis on 34 specimens (including 22 HCHST composite columns, 4 CFST composite columns and 8 HCST composite columns) subjected to eccentrical compression load are carried out by ABAQUS software. The effects of different parameters on the N-μ_m curves are discussed. The main parameters varied in this paper are: 1) the cubic compressive strength of concrete (f_{cu}); 2) the yield strength of steel tube (f_y); 3)

FIGURE 2
Comparison for different constitutive models of concrete.
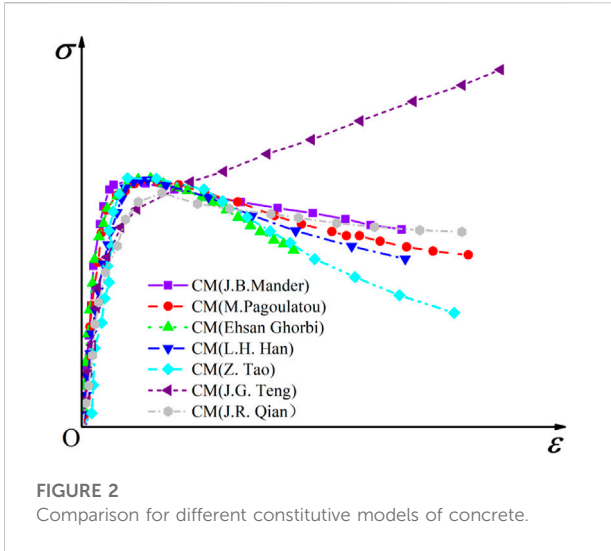
the thickness of tube wall (t); 4) eccentricity (e); 5) the slenderness ratio (λ).

The cubic compressive strength of concrete (f_{cu})

The comparison of N-μ_m curves for specimens with different f_{cu} when the eccentricity is 30 mm and 50 mm is shown in Figures 6A,B, respectively. The ultimate eccentrical compression bearing capacity (N_a) and mid-span deflection with different f_{cu} are summarized in Table 3. We can see from Figure 6A; Table 3, when an eccentricity is equal to 50 mm, and f_{cu} increases from 40 to

60 Mpa, 80 and 100 MPa, respectively, N_a of specimens increases from 1,603.26 to 1,704.57 kN, 1,890.17 and 2,015.58 kN in turn, which increases by 6.3%, 15.2%, 21.5%, respectively. On the contrary the mid-span deflection decreases from 40.01 to 39.94 mm, 39.62 and 39.31 mm in turn, which decreases by 0.2%, 1.0%, and 1.8%, respectively. As shown in Figure 6B; Table 3, when an eccentricity is equal to 30 mm, and f_{cu} increases from 40 to 60 Mpa, 80 and 100 MPa, respectively, N_a of specimens increases from 2,015.23 to 2,116.48 kN, 2,351.03 and 2,506.09 kN in turn, which increases by 4.8%, 15.3%, and 19.6%, respectively. On the contrary the mid-span deflection decreases from 41.76 to 41.69 mm, 41.57 and 41.52 mm in turn, which decreases by 0.2%, 0.5%, and 0.6%, respectively. It can be concluded that compared with the specimens adopting ordinary concrete, N_a of specimens using HPC is improved significantly, and the curves drop faster after peak load, while it has little effect on the lateral stiffness of the specimens for using HPC.

The yield strength of steel tube (f_y)

The comparison of N-μ_m curves for specimens with the different f_y when the eccentricity is 30 and 50 mm is shown in Figures 6C,D, respectively. N_a and mid-span deflection with different f_y are summarized in Table 3. As shown in Figure 6C; Table 3, when an eccentricity is equal to 50 mm, and f_y increases from 335 to 400 MPa, 500 and 700 MPa, respectively, N_a of specimens increases from 1,852.45 to 2,015.58 kN, 2,260.16 and 2,800.31 kN in turn, which increases by 8.1%, 18.1%, and 33.9%, respectively. On the contrary the mid-span deflection decreases from 39.98 to 39.31 mm, 38.58 and 37.81 mm in turn, which decreases by 1.7%, 3.6%, and 5.5%, respectively. As shown in Figure 6D; Table 3, when an
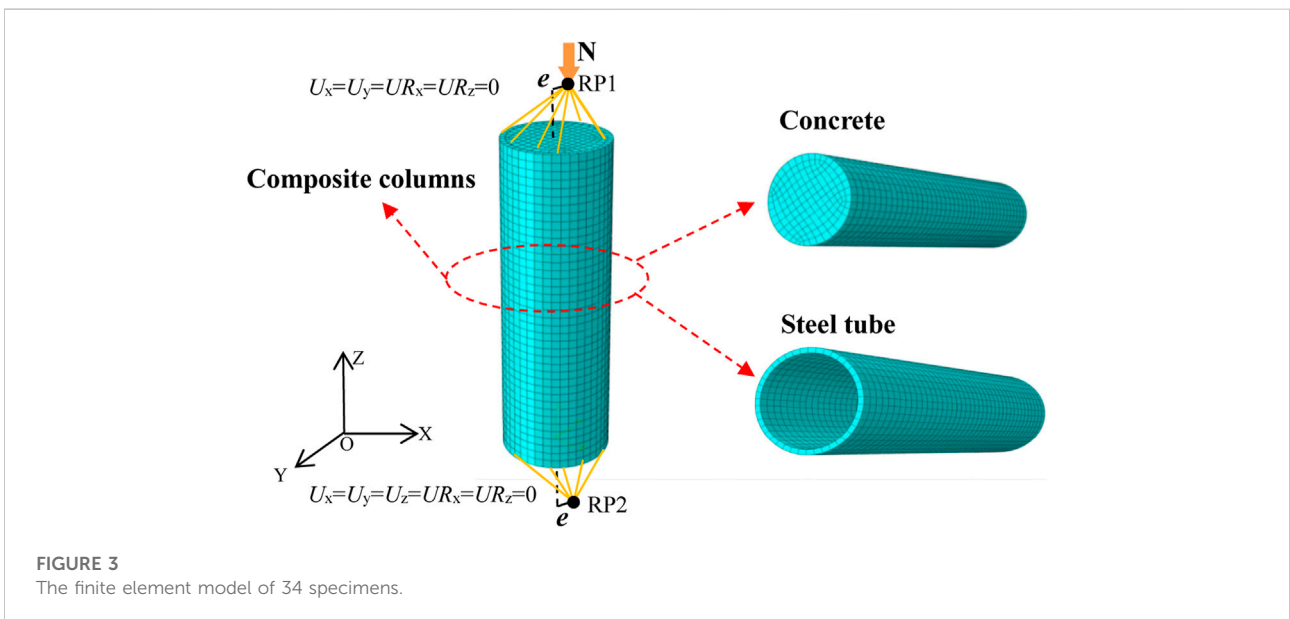

FIGURE 3
The finite element model of 34 specimens.

TABLE 2 Comparison between N_a and N_t

Specimens		D/mm	t/mm	L/mm	f_y/MPa	$f_{cu,k}$/MPa	e/mm	N_a/kN	N_t/kN	$\left|\frac{N_t - N_a}{N_t}\right| \times 100\%$
Test (Wang et al., 2013)	CSCA-1	108	4	324	370	96	0	1,123.6	1,221.8	8.7
	CSCA-2	108	6	324	381	96	0	1,417.1	1,562.9	9.4
	CSCA-3	108	8	324	385	96	0	1,836.6	1,847.5	1.8
	CSCB-1	133	4	399	398	96	0	1,632.1	1,638.2	1.4
	CSCB-2	133	6	399	392	96	0	1,840.9	2,001.7	8.1
	CSCB-3	133	8	399	398	96	0	2,224.7	2,328.3	4.5
	CSCC-1	159	4	477	393	96	0	2,224.3	2,358.5	5.7
	CSCC-2	159	6	477	396	96	0	2,635.3	2,684.5	0.5
	CSCC-3	159	8	477	387	96	0	3,070.7	2,986.7	2.8
Test (Lee et al., 2019)	E48-30	480	6	1440	468	50	240	3,339.1	3,287.4	1.2
	E48-60	180	6	800	275	30	120	3,777.5	3,857.3	2.1
	E60-30	180	6	600	275	30	60	4,640.5	4,850.9	4.5
Test (Yu et al., 2007)	C150-4	100	1.9	1500	404	120	15	408.5	434.4	6.3
	C150-6	100	1.9	1500	404	120	30	312.7	323.5	3.5
Test (Han and Yao, 2004)	LCSC2-1	200	3	2000	400	40	30	1,297.3	1,215.4	6.8
	LCH2-1	200	3	2000	400	40	30	1,297.3	1,291.7	0.9

Note: $f_{cu,k}$ is the standard value of concrete cubic compressive strength.

eccentricity is equal to 30 mm, and f_y increases from 335 to 400 MPa, 500 and 700 MPa, respectively, N_a of specimens increases from 2,298.86 to 2,506.09 kN, 2,817.75 and 3,459.25 kN in turn, which increases by 8.2%, 18.5%, and 33.6%, respectively. On the contrary the mid-span deflection decreases from 42.09 to 41.52 mm, 41.01 and 40.51 mm in turn, which decreases by 1.4%, 2.6%, and 3.8%, respectively. It can be concluded that compared with the specimens using ordinary steel tube, N_a of specimens using HST is improved significantly, and the curves drop more slowly after peak load, and the load-holding (Ji et al., 2020) capacity increases gradually, while it has little effect on the lateral stiffness of the specimens for using HST. The restraint effect of HST on concrete is stronger than ordinary steel tube.

The thickness of tube wall (t)

The comparison of N-μ_m curves for specimens with different t when the eccentricity is 30 and 50 mm is shown in Figures 6E,F, respectively. N_a and mid-span deflection with different t are summarized in Table 3. As shown in Figure 6E; Table 3, when an eccentricity is equal to 50 mm, and t increases from 2 to 4 mm, 6 mm, 8 mm, and 10 mm, respectively, N_a of specimens enhances from 1,626.09 to 2,202.36 kN, 2,800.31 kN, 3,457.89 kN, and 4076.62 kN in turn, which increases by 26.2%, 34.9%, 53%,

and 61%, respectively. On the contrary the mid-span deflections decreases from 41.06 to 38.61 mm, 37.81 mm, 37.55 mm, and 37.37 mm in turn, which decreases by 5.9%, 8.0%, 8.5%, and 8.9%, respectively. As shown in Figure 6F; Table 3, when an eccentricity is equal to 30 mm, and t increases from 2 to 4 mm, 6 mm, 8 mm, and 10 mm, respectively, N_a of specimens enhances from 2,076.86 to 2,794.29 kN, 3,424.41 kN, 4,253.57 kN, and 5,006.29 kN in turn, which increases by 26.7%, 39.5%, 51.2%, and 59.6%, respectively. On the contrary the mid-span deflections decreases from 42.90 to 41.11 mm, 40.51 mm, 40.47 mm, and 40.45 mm in turn, which decreases by 4.2%, 5.6%, 5.7%, and 5.8%, respectively. It can be concluded that with the increasing of t, N_a of the HCHST composite columns increases obviously, and the curves drop more slowly after peak load, and the load-holding capacity increases progressively, while mid-span deflection reduces gradually, so the lateral stiffness (Ji et al., 2022) of the specimens can be improved by increasing t.

The eccentricity (e)

The comparison of N-μ_m curves for specimens with different e when t is 4 and 10 mm is shown in Figures 6G,H, respectively. N_a and mid-span deflection with different e are summarized in
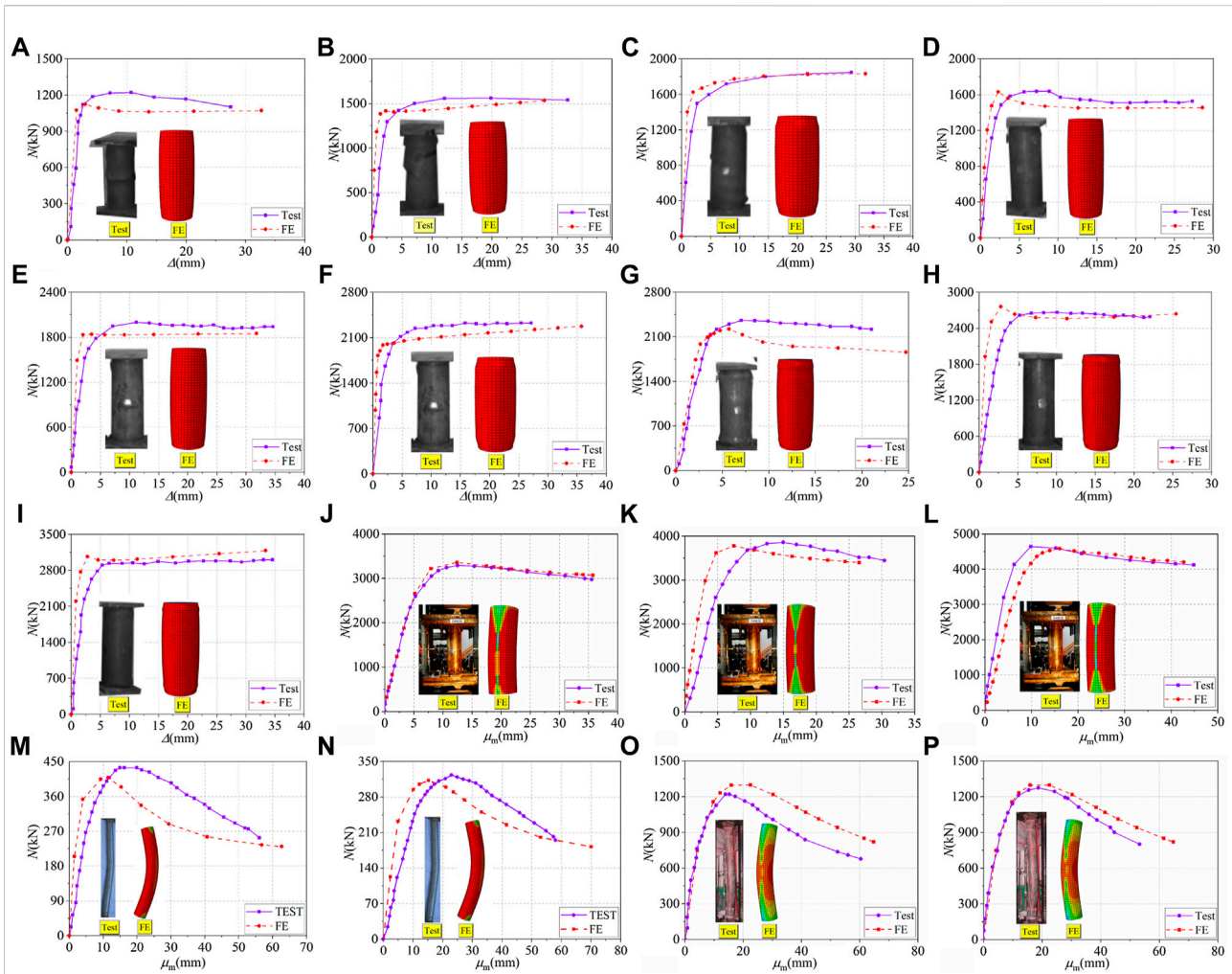
FIGURE 4
Compression for N-Δ and N-μ_m curves between simulation and test results: **(A)** CSCA-1; **(B)** CSCA-2; **(C)** CSCA-3; **(D)** CSCB-1; **(E)** CSCB-2; **(F)** CSCB-3; **(G)** CSCC-1; **(H)** CSCC-2; **(I)** CSCC-3; **(J)** E40-30; **(K)** E40-60; **(L)** E60-30; **(M)** C150-4; **(N)** C150-6; **(O)** LCSC2-1; **(P)** LCH2-1.
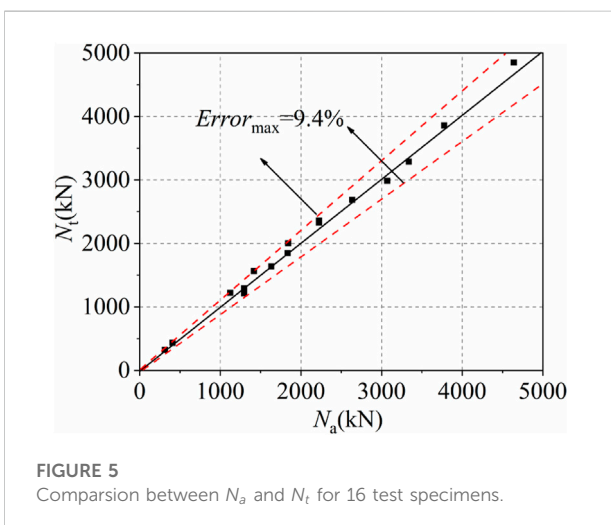

FIGURE 5
Comparsion between N_a and N_t for 16 test specimens.

Table 3. As shown in Figure 6G; Table 3, when t is equal to 10 mm, and e increases from 30 to 40 mm, 50 mm, 60 mm, 70 mm, and 80 mm, respectively, N_a of specimens decreases from 5,006.29 to 4,517.29 kN, 4,076.62 kN, 3,675.65 kN, 3,358.71 kN, and 3,078.13 kN in turn, which decreases by 11.2%, 19.1%, 27.3%, 34.2%, and 39.5% ,respectively. The mid-span deflection decreases from 40.45 to 38.90 mm, 37.37 mm, 35.77 mm, 34.21 mm, and 32.56 mm in turn, which decreases by 3.7%, 7.5%, 11.4%, 14.3%, and 19.4%, respectively. As shown in Figure 6H; Table 3, when t is equal to 4 mm, and e increases from 30 to 40 mm, 50 mm, 60 mm, 70 mm, and 80 mm, respectively, N_a of specimens decreases from 2,794.29 to 2,467.24 kN, 2,202.36 kN, 1,979.51 kN, 1,798.82 kN, and 1641.86 kN in turn, which decreases by 11.8%, 21.9%, 28.5%, 35.7%, and 39.5%, respectively. The mid-span deflection decreases from 41.11 to 39.97 mm, 38.61 mm, 37.33 mm, 35.72 mm, and 34.39 mm in turn, which decreases by 2.8%,
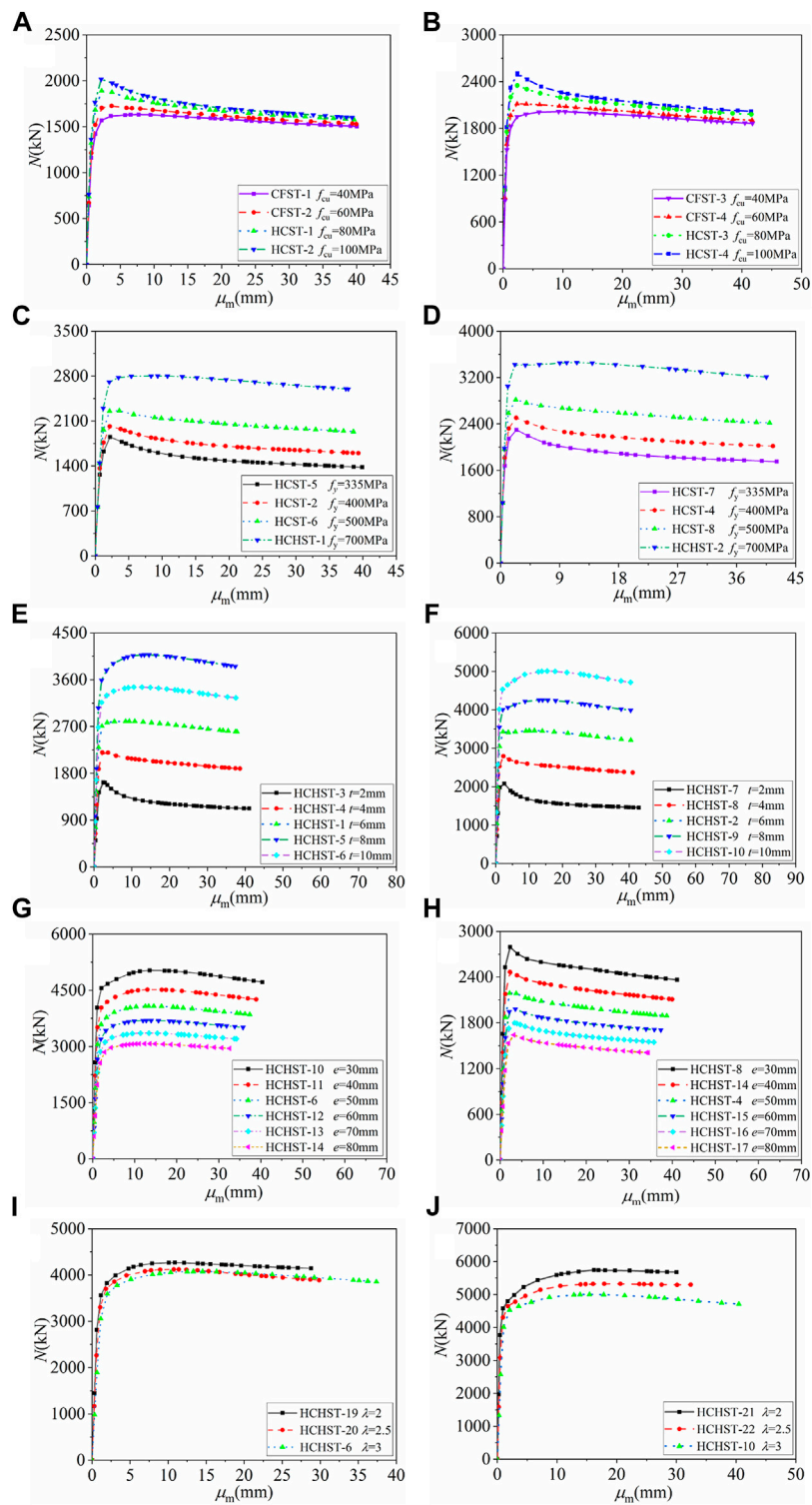
FIGURE 6
Comparison of N-μ_m curves with different parameters. **(A)** Different f_{cu} when e = 30 mm; **(B)** Different f_{cu} when e = 50 mm; **(C)** Different f_y when e = 30 mm; **(D)** Different f_y when e = 50 mm; **(E)** Different t when e = 30 mm; **(F)** Different t when e = 50 mm; **(G)** Different e when t = 4 mm; **(H)** Different e when t = 10 mm; **(I)** Different λ when e = 30 mm; **(J)** Different λ when e = 50 mm.

TABLE 3 The ultimate eccentrical compression bearing capacity and mid-span lateral deflection of 34 specimens.

Specimens	D/mm	t/mm	L/mm	f_{cu}/MPa	f_y/MPa	e/mm	λ	N_a/kN	μ_m/mm
CFST-1	200	6	600	40	400	50	3	1,603.26	40.01
CFST-2	200	6	600	60	400	50	3	1,704.57	39.94
CFST-3	200	6	600	40	400	30	3	2,015.23	41.76
CFST-4	200	6	600	60	400	30	3	2,116.48	41.69
HCST-1	200	6	600	80	400	50	3	1,890.17	39.62
HCST-2	200	6	600	100	400	50	3	2,015.58	39.31
HCST-3	200	6	600	80	400	30	3	2,351.03	41.57
HCST-4	200	6	600	100	400	30	3	2,506.09	41.52
HCST-5	200	6	600	100	335	50	3	1,852.45	39.98
HCST-6	200	6	600	100	500	50	3	2,260.16	38.58
HCST-7	200	6	600	100	335	30	3	2,298.86	42.09
HCST-8	200	6	600	100	500	30	3	2,817.75	41.01
HCHST-1	200	6	600	100	700	50	3	2,800.31	37.81
HCHST-2	200	6	600	100	700	30	3	3,459.25	40.51
HCHST-3	200	2	600	100	700	50	3	1,626.09	41.06
HCHST-4	200	4	600	100	700	50	3	2,202.36	38.61
HCHST-5	200	8	600	100	700	50	3	3,457.89	37.55
HCHST-6	200	10	600	100	700	50	3	4,076.62	37.37
HCHST-7	200	2	600	100	700	30	3	2,076.86	42.90
HCHST-8	200	4	600	100	700	30	3	2,794.29	41.11
HCHST-9	200	8	600	100	700	30	3	4,253.57	40.47
HCHST-10	200	10	600	100	700	30	3	5,006.29	40.45
HCHST-11	200	10	600	100	700	40	3	4,517.29	38.90
HCHST-12	200	10	600	100	700	60	3	3,675.65	35.77
HCHST-13	200	10	600	100	700	70	3	3,358.71	34.21
HCHST-14	200	10	600	100	700	80	3	3,075.13	32.56
HCHST-15	200	4	600	100	700	40	3	2,467.24	41.11
HCHST-16	200	4	600	100	700	60	3	1,979.51	37.33
HCHST-17	200	4	600	100	700	70	3	1,798.82	35.72
HCHST-18	200	4	600	100	700	80	3	1,641.86	34.39
HCHST-19	200	10	400	100	700	50	2	4,254.56	28.79
HCHST-20	200	10	500	100	700	50	2.5	4,120.71	29.84
HCHST-21	200	10	400	100	700	30	2	5,474.33	30.09
HCHST-22	200	10	500	100	700	30	2.5	5,326.88	32.40

5.9%, 8.8%, 13.2%, and 16.4%, respectively. It can be concluded that with the increasing of e, N_a of the HCHST composite columns decreases gradually, and mid-span deflection decreases accordingly.

The slenderness ratio (λ)

The comparison of N-μ_m curves for specimens with different λ when e is 30 and 50 mm is shown in Figures 6I,J, respectively. N_a and mid-span deflection with different λ are summarized in Table 3. As shown in Figure 6I; Table 3, when e is equal to 50 mm, and λ increases from 2 to 2.5 and

3 in turn, N_a decreases from 4,254.56 to 4,120.71 kN, 4,076.62 kN, respectively, which decreases by 3.2% and 4.2%, respectively. While the mid-span deflection increases from 28.79 to 29.84 mm and 37.37 mm in turn, which increases by 3.6% and 18.8%, respectively. As shown in Figure 6J; Table 3, when e is equal to 30 mm, and λ increases from 2 to 2.5 and 3 in turn, N_a decreases from 5,474.33 to 5,326.68 kN, 5,001.72 kN, respectively, which decreases by 2.8%, 8.7%, respectively. While the mid-span deflection increases from 30.09 to 32.40 mm and 40.45 mm in turn, which increases by 7.2% and 25.7%, respectively. It can be concluded that with the increasing of λ, N_a of the
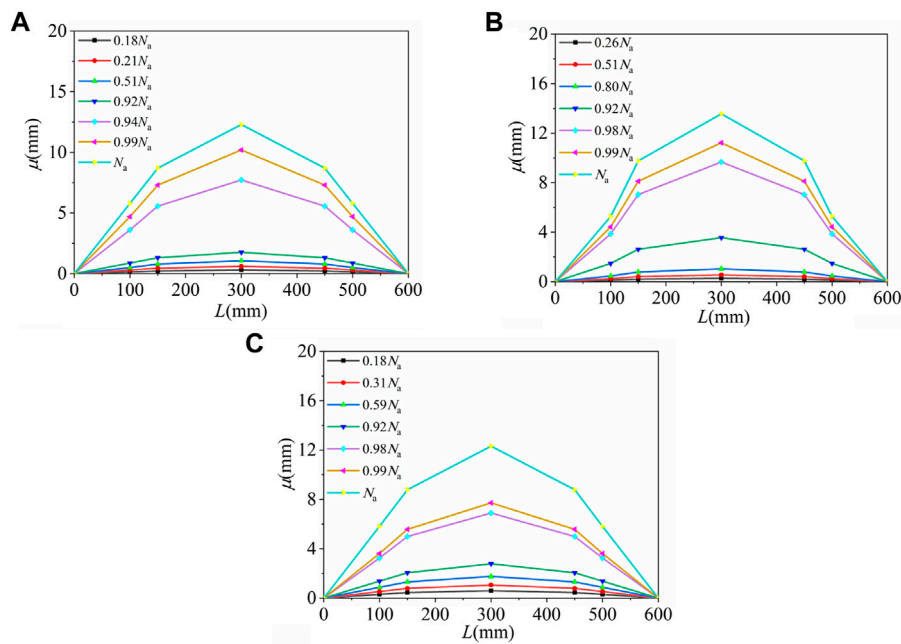
FIGURE 7
Lateral deflection curves for three typical specimens. **(A)** HCHST-10; **(B)** HCHST-6; **(C)** HCHST-14.

HCHST composite columns decreases gradually, on the contrary the lateral deflection increases obviously.

Lateral deflection curves of high-performance concrete-filled high-strength steel tube composite columns

Lateral deflection curves of three typical specimens [HCHST-10 (e = 50 mm), HCHST-6 (e = 30 mm) and HCHST-14 (e = 80 mm)] are shown in Figure 7. It can be seen that when the load increases gradually from zero to 0.92 N_a, the deflection along with the height of the composite columns is negligible, however the deflection increases significantly when the load increases gradually from 0.92 N_a to peak load. Under eccentrical compression load, the deflection curves along with the height of the composite columns are almost in the shape of a half-sine wave (Ji et al., 2022), and the deflection relationship of various points can be expressed by Eq. 3 (Mao et al., 2021):

$$\mu = \mu_a \sin \frac{\pi Z}{L} \tag{3}$$

Where μ_a is the deflection of the composite columns under various loads; Z is the distance between each point on the

specimens and the mid-span; L is the height of the composite columns.

Load-strain curves of high-performance concrete-filled high-strength steel tube composite columns

The load (N) versus strain (ε) relationships of the mid-span section for three typical specimens [HCHST-10 (e = 50 mm), HCHST-6 (e = 30 mm) and HCHST-14 (e = 80 mm)] are shown in Figure 8. In this paper, it is asummed that the tensile strain is positive and the compressive strain is negative. It can be seen that in the initial of loading, the strain of each parts of HCHST composite columns changed linearly, thereby indicating that the composite columns were at the elastic stage. When the load increased to 80% of the peak load, the longitudinal strain begins to grow non-linearly. When the load increases to the peak load, the steel tube reaches yield strength, and then the strain increases rapidly until the specimen is damaged. As shown in Figure 8, with the increasing of the eccentricity, the decline rate of the load-strain curves after peak load decreases gradually. High-strength steel tubes of each specimen can reach yield strength, and the high-strength steel tubes can make full use of the restraint effect when the HCHST composite columns are subjected to the eccentric compression load.
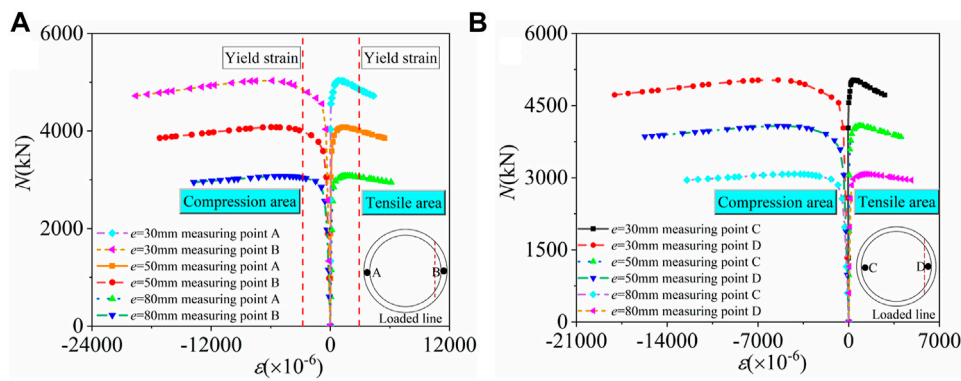
FIGURE 8
N-ε curves with different eccentricity: **(A)** Load-strain curves of steel tube; **(B)** Load-strain curves of concrete.
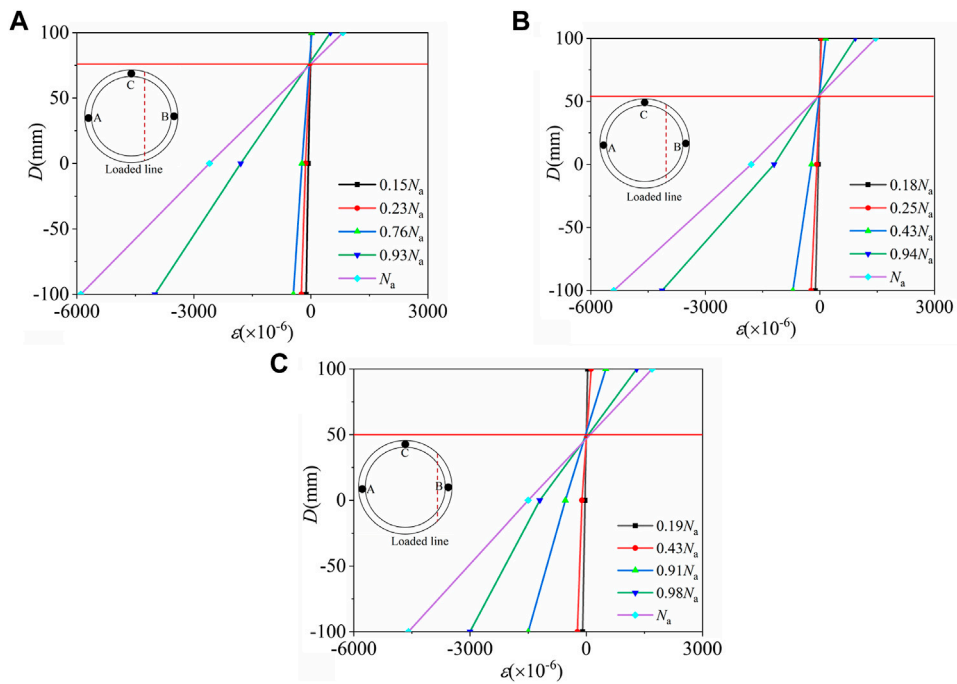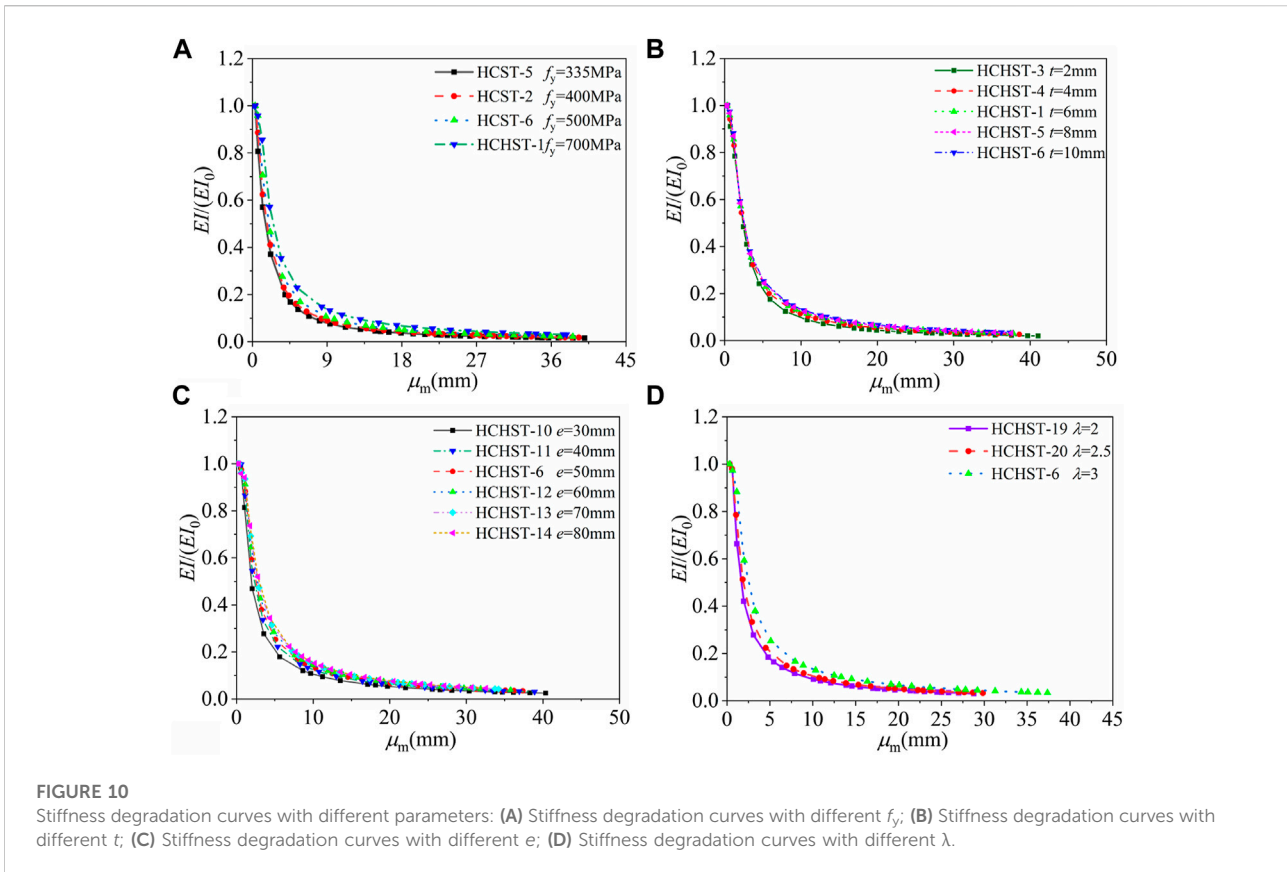

FIGURE 9
Longitudinal strain distribution curves of mid-span sections for three typical specimens: **(A)** HCHST-10; **(B)** HCHST-6; **(C)** HCHST-14.

Verification of the plane section assumption

In order to make clear whether the HCHST composite columns satisfy the plane cross-section assumption. Three typical specimens [HCHST-10 (*e* = 50 mm), HCHST-6 (*e* = 30 mm) and HCHST-14 (*e* = 80 mm)] are selected from

22 HCHST composite columns, and the longitudinal strain distribution curves of its mid-span section are drawn as shown in Figure 9. It can be seen that longitudinal strain curves of the mid-span section show insignificant differences with the gradual increase of load. The strain varies linearly along with the height of the section, which shows that the mid-span section accords with the plane cross-section assumption.

FIGURE 10
Stiffness degradation curves with different parameters: **(A)** Stiffness degradation curves with different f_y; **(B)** Stiffness degradation curves with different t; **(C)** Stiffness degradation curves with different e; **(D)** Stiffness degradation curves with different λ.

Stiffness degradation of specimens

The lateral deflection curve of the HCHST composite columns presents sinusoidal half-wave distribution. The stiffness of HCHST composite columns subjected to eccentrical compression load can be expressed as:

$$EI = \frac{NeL^2}{\pi^2 \mu_m} \qquad (4)$$

Where EI is the secant bending stiffness (kN·m²); N is the eccentrical compression load (kN); e is the eccentricity (mm); L is the height of specimens (mm); μ_m is the mid-span deflection of the specimens (mm).

The HCHST composite columns are accompanied by material destruction in the loading process, resulting in a gradual decrease in the effective stress area of the cross-section of the composite columns and the comprehensive deformation modulus of materials. So the flexural stiffness of composite columns cannot keep a constant value but decreases gradually with the increasing of lateral deflection. According to Eq. 4, stiffness degradation curves of specimens with different parameters are given in Figure 10. The vertical ordinate in the Figure 10 is the ratio of secant stiffness (EI) to initial stiffness (EI_0). It can be seen from Figure 10 that the element is in the elastic location at the initial loading stage, and the stiffness does not vary. With the increasing of N, the specimens enter the elastic-plastic stage, at which the stiffness begins to decrease with the rein creasing of deflection. The stiffness degradation curves with different f_y and t are shown in Figures 10A,B, it can be concluded that with the increasing of f_y and t, the restraint effect of steel tube on high-performance concrete is improved, the flexibility of the specimens increases, the stiffness degradation rate reduces. The stiffness degradation curves with different e are shown in Figure 10C, it can be concluded that with the increasing of e, the stiffness of the specimens increase gradually. The stiffness degradation curves with different λ are shown in Figure 10D, it can be concluded that with the increasing of λ, the material failure degree of the specimen decreases gradually, and the stiffness increases.

Failure mechanism of high-performance concrete-filled high-strength steel tube composite columns

The longitudinal stress distribution and longitudinal strain distribution diagram of concrete and steel tube in
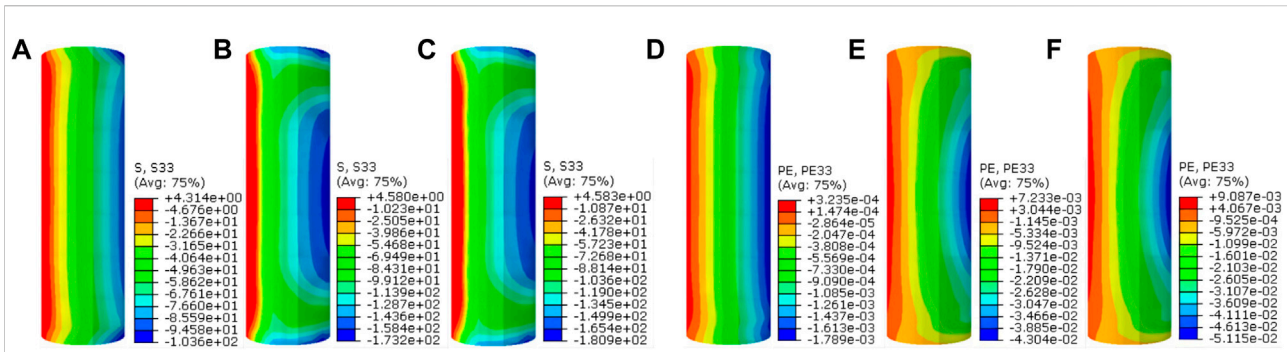
FIGURE 11
Distribution of longitudinal stresses and longitudinal strains of concrete at each loading stages of typical specimen HCHST-6: **(A)** Longitudinal stress distribution of concrete at elastic stage; **(B)** Longitudinal stress distribution of concrete at elastic-plastic stage; **(C)** Longitudinal stress distribution of concrete at plastic stage; **(D)** Longitudinal strain distribution diagram of concrete at elastic stage; **(E)** Longitudinal strain distribution diagram of concrete at elastic-plastic stage; **(F)** Longitudinal strain distribution diagram of concrete at plastic stage.
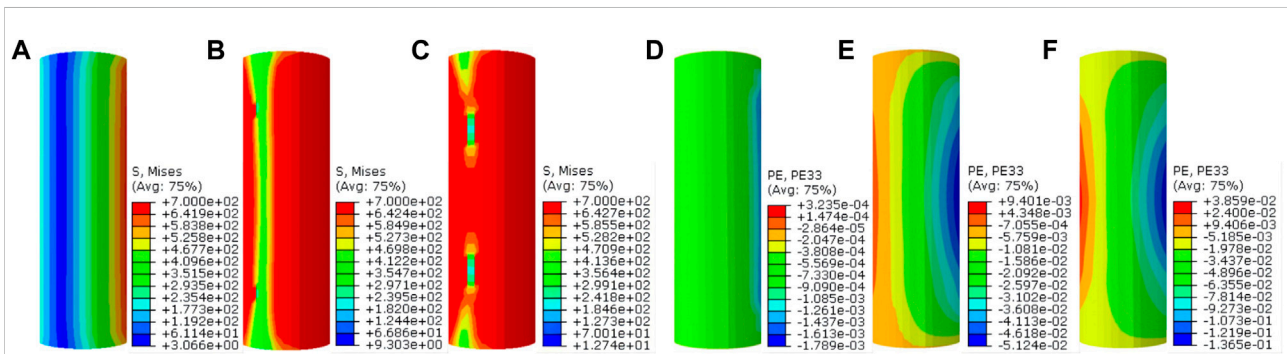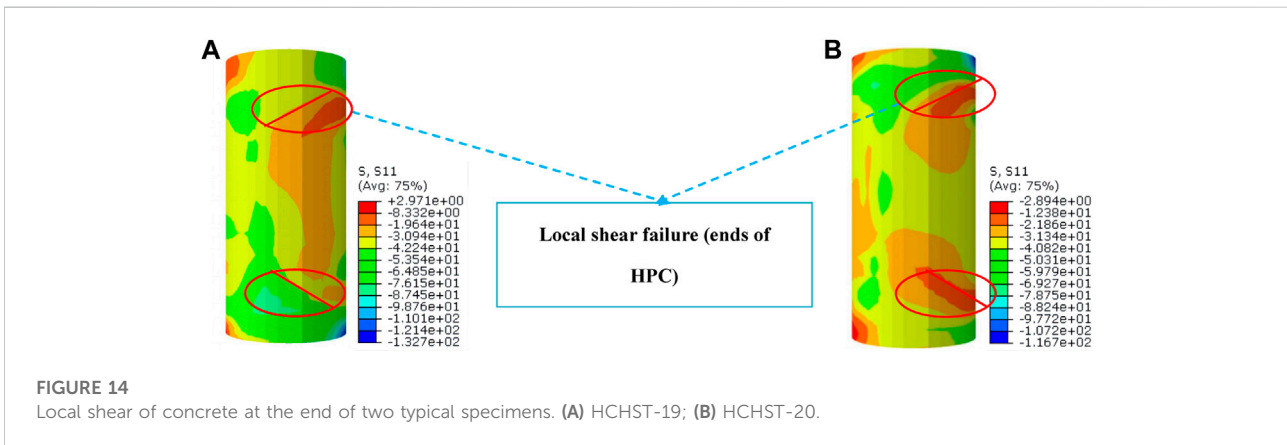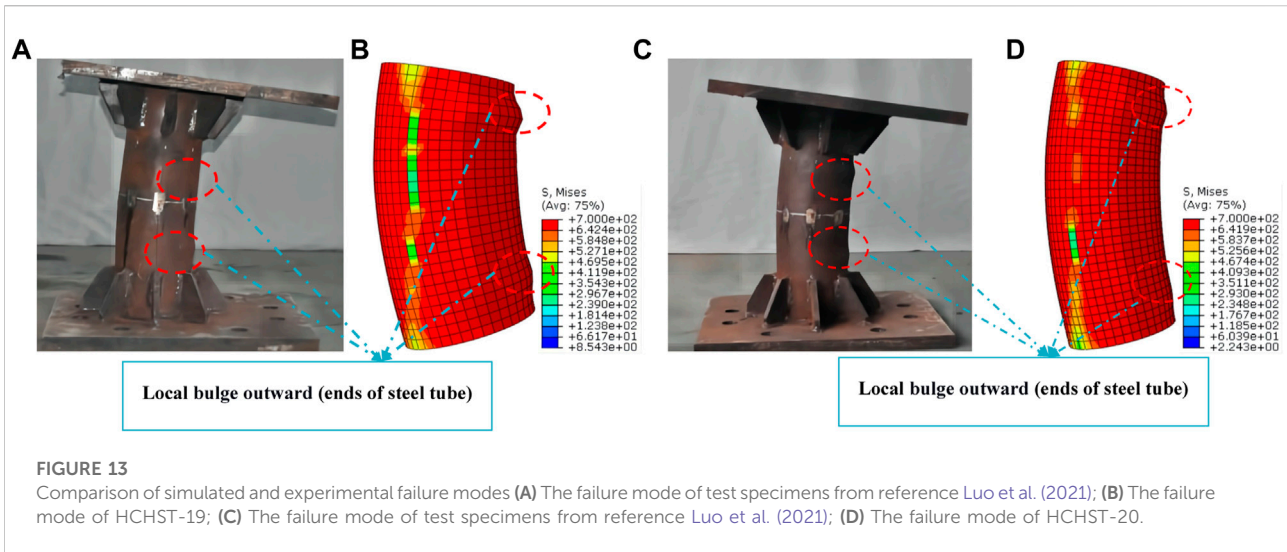

FIGURE 12
Distribution of MIES stresses and longitudinal strains of steel tubes at each loading stage of typical specimen HCHST-6: **(A)** The MISES stress distribution of steel tube at elastic stage; **(B)** The MISES stress distribution of steel tube at elastic-plastic stage; **(C)** The MISES stress distribution of steel tube at plastic stage; **(D)** Longitudinal strain distribution diagram of steel tube at elastic stage; **(E)** Longitudinal strain distribution diagram of steel tube at elastic-plastic stage. **(F)** Longitudinal strain distribution diagram of steel tube at plastic stage.

each loading stage of typical specimen HCHST-6 are shown in Figures 11, 12. During the initial stage of loading, the HCHST composite columns can be considered to be at the elastic work stage. With the increasing of load gradually, the longitudinal stress of the steel tube is approximately distributed in a band, the stress on the compression side of the steel tube is greater than that on the tension side, and the steel tube reaches the proportional limit. At this time, there is less contact between the steel tube and the concrete, each component were almost in independent working stage, the concrete is stressed evenly, the longitudinal stress is distributed in a band, and the specimen is in a compressed state as a whole. When the load increased to 80% of peak load, composite columns begin to enter the elastic-plastic stage, and the steel tube enters the yield stage. When the specimen reaches the peak load, the plastic strain in the concrete compression area begins to concentrate to the mid-span section, the stress

concentration occurs at the upper and lower ends of the concrete compression side, and the stress on the compression side is significantly greater than that on the tensile side. When the specimens reach the peak load, the HCHST composite columns begin to enter the plastic stage with the gradual increasing of deflection, and the steel tube in the tension area in the compression area reaches the yield strength. And the steel tube begin to buckling failure occurs at the end of the test specimens, as shown in Figure 13. Due to the local buckling of the end of steel tube, the transverse restraint effect of the steel tube on the concrete in this area is reduced, resulting in local shear failure of the concrete in this area, as shown in Figure 14. With the increasing of deflection, cracks occur in the concrete tension area, when the load dropped to 85% of the peak load, the area of concrete tension zone increases, most steel tube in tension zone and compression zone reach yield strength.

FIGURE 13
Comparison of simulated and experimental failure modes **(A)** The failure mode of test specimens from reference Luo et al. (2021); **(B)** The failure mode of HCHST-19; **(C)** The failure mode of test specimens from reference Luo et al. (2021); **(D)** The failure mode of HCHST-20.

FIGURE 14
Local shear of concrete at the end of two typical specimens. **(A)** HCHST-19; **(B)** HCHST-20.

Bearing capacity of high-performance concrete-filled high-strength steel tube composite columns subjected to eccentric load

The ultimate bearing capacity formula of HPC-filled steel tube (HCST) composite stub columns under axial load has been put forward by Yu et al. (2002):

$$N_1 = A_c f_{cu,k} \left(1 + 1.8\rho \right) \qquad (5)$$

Where, A_c is the cross-sectional area; $f_{cu,k}$ is the standard value of cubic compressive strength of concrete; ρ is the coefficient of confinement effect.

The ultimate bearing capacity of CFST stub columns subjected to eccentrical load is usually expressed in the form of axial force-moment equation, but this kind of expression is not suitable for engineering application. Therefore, in order to

facilitate the application of engineering, the eccentricity reduction coefficient (φ_1) and the slenderness ratio reduction coefficient (φ_2) of the HCHST composite columns are introduced as shown in Eq. 6. Based on finite element analysis data, φ_1 and φ_2 can be acquired by statistical regression as shown in Eqs 7–10.

$$N_u = \varphi_1 \varphi_2 \, A_c \, f_{cu,k} \left(1 + 1.8\rho \right) \qquad (6)$$

$$\varphi_1 = 0.11\alpha^2 - 0.6\alpha + 0.73 \qquad (7)$$

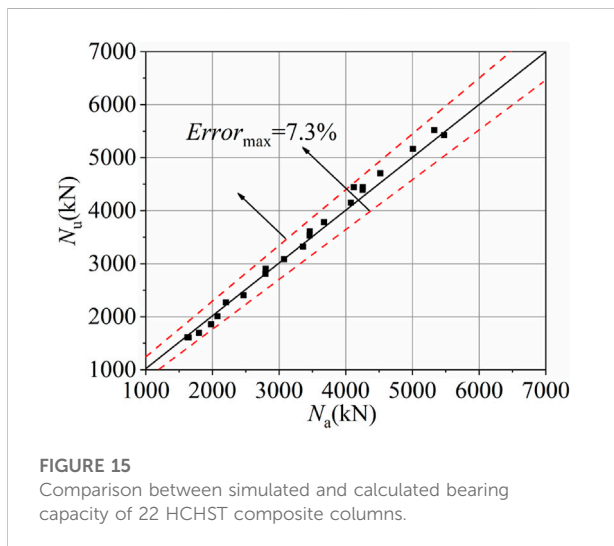$$\alpha = e/r \qquad (8)$$

$$\rho = f_y A_s \big/ f_{cu,k} A_c \qquad (9)$$

$$\varphi_2 = -0.66\delta^2 + 0.89\delta + 0.77 \qquad (10)$$

Where, r is the radius of the circular section; f_y is the yield strength of the high-strength steel tube; A_s is the cross-sectional area of the high-strength steel tube. λ is the slenderness ratio and δ is equal to $\lambda/3$.

TABLE 4 Comparison between N_a and N_u for 22 high-performance concrete-filled high-strength steel tube composite columns.

Specimens	e/mm	λ	ρ	δ	α	φ_1	φ_2	N_a/kN	N_u/kN	$\left\|\frac{N_u-N_a}{N_u}\right\| \times 100\%$
HCHST-1	50	3	1.37	1	0.5	0.45	1	2,800.31	2,900.81	3.5
HCHST-2	30	3	1.37	1	0.3	0.56	1	3,459.25	3,609.90	4.2
HCHST-3	50	3	0.43	1	0.5	0.45	1	1,626.09	1,613.69	0.3
HCHST-4	50	3	0.88	1	0.5	0.45	1	2,202.36	2,269.45	3.9
HCHST-5	50	3	1.89	1	0.5	0.45	1	3,457.89	3,529.09	2.1
HCHST-6	50	3	2.45	1	0.5	0.45	1	4,076.62	4,150.68	1.8
HCHST-7	30	3	0.43	1	0.3	0.56	1	2,076.86	2,008.25	3.4
HCHST-8	30	3	0.88	1	0.3	0.56	1	2,794.29	2,807.03	0.5
HCHST-9	30	3	1.89	1	0.3	0.56	1	4,253.57	4,391.76	3.2
HCHST-10	30	3	2.45	1	0.3	0.56	1	5,006.29	5,165.29	3.1
HCHST-11	40	3	2.45	1	0.4	0.51	1	4,517.29	4,704.11	0.6
HCHST-12	60	3	2.45	1	0.6	0.41	1	3,675.65	3,781.73	3.1
HCHST-13	70	3	2.45	1	0.7	0.36	1	3,358.71	3,320.55	2.7
HCHST-14	80	3	2.45	1	0.8	0.32	1	3,075.13	3,084.23	0.3
HCHST-15	40	3	0.88	1	0.4	0.51	1	2,467.24	2,402.79	0.3
HCHST-16	60	3	0.88	1	0.6	0.41	1	1,979.51	1,856.28	6.3
HCHST-17	70	3	0.88	1	0.7	0.36	1	1,798.82	1,697.71	5.6
HCHST-18	80	3	0.88	1	0.8	0.32	1	1,641.86	1,609.78	2.1
HCHST-19	50	2	2.45	0.67	0.5	0.45	1.07	4,254.56	4,441.29	4.2
HCHST-20	50	2.5	2.45	0.83	0.5	0.45	1.05	4,120.71	4,441.27	7.3
HCHST-21	30	2	2.45	0.67	0.5	0.56	1.07	5,474.33	5,423.55	1.0
HCHST-22	30	2.5	2.45	0.83	0.5	0.56	1.05	5,326.88	5,517.23	5.1

FIGURE 15
Comparison between simulated and calculated bearing capacity of 22 HCHST composite columns.

Equation 6 is used to calculate the ultimate bearing capacity (N_u) of 22 HCHST composite columns under eccentrical load, as shown in Table 4; Figure 15. N_a stands for the simulated bearing capacity of HCHST composite columns under eccentrical load in Table 4, and by comparison it can be seen that the maximum error ($Error_{max}$) between N_u and N_a is 7.3%, which can meet the requirements of engineering precision.

Conclusion

The finite element models of 22 HCHST composite columns, 4 CFST composite columns and 8 HCST composite columns subjected to eccentrical load are established by ABAQUS software. The load-deflection curves of the specimens are obtained during the whole process. The effect of different parameters on the ultimate eccentric compression bearing capacity of specimens is discussed. The calculation formula which is suitable for the eccentric bearing capacity of the HCHST composite columns is deduced by statistical regression. The specific conclusions can be drawn as follows:

1) Based on the simplified constitutive model of steel and the constrained concrete constitutive model, the numerical simulation of 34 stub columns subjected to eccentric load was conducted by ABAQUS software. The load-displacement curves and failure modes of specimens were obtained. By comparing with the test data, it could be found that the curves were in good agreement, and the failure modes were similar.

The rationality of the constitutive model of materials and modeling method was verified.

2) Compared with the specimens using ordinary concrete, the specimens using HPC exhibit brittle behavior. The restraint effect of high-strength steel tube on HPC is stronger than ordinary steel tube, and high-strength steel tube with thick wall is more suitable for the HCHST composite columns. With the increasing of steel tube wall thickness, the ultimate bearing capacity of the HCHST composite columns is continuously improved. In contrast, the mid-span lateral deflection of composite columns is gradually reduced. With the increasing of the eccentricity and the slenderness ratio, the ultimate bearing capacity of the HCHST composite columns subjected to eccentrical load decreases by degrees.

3) With the increasing of steel tube wall thickness and eccentricity, the stiffness degradation rate of HCHST composite columns decreases gradually and the ductility of HCHST composite columns increases by degrees. The longitudinal strain distribution curve of mid-span section of HCHST composite columns is linear with the increasing of compression load, which meets the plane section assumption. The main failure modes of HCHST composite columns under eccentrical compression load include buckling at the end of steel tubes and shear failure at the end of concrete. The restraint effect of high-strength steel tube on HPC is stronger compared with ordinary steel tube.

4) Based on the existing ultimate axial compression bearing capacity formula of HPC-filled steel tube stub columns, the eccentricity reduction coefficient (φ_1) and the slenderness ratio reduction coefficient (φ_2) are introduced, and the ultimate bearing capacity formula of HCHST composite columns under eccentrical load is proposed by statistics regression. The maximum error is 7.3%, which can meet the demand of engineering accuracy.

Data availability statement

The original contributions presented in the study are included in the article/Supplementary Material, further inquiries can be directed to the corresponding authors.

Author contributions

LJ: Finite element simulation, writing; WW: Finite element simulation, writing; JJ: Translation; HR: Translation; QW: Writing; RS: Translation; CY: Writing; HZ and GL: Writing. All authors contributed to the article and approved the submitted version.

Funding

Conflict of interest

QW was employed by China Academy of Building Research Co., Ltd.

The remaining authors declare that the research was conducted in the absence of any commercial or financial relationships that could be construed as a potential conflict of interest.

Publisher's note

References

American Concrete Institute (2005). *Building code requirements for structural concrete and commentary, ACI 318-05*. Farmington Hills (MI), Detroit, USA: American Concrete Institute.

Cai, Z. W., Liu, F. C., Yu, J. T., Yu, K. Q., and Tian, L. K. (2021). Development of ultra-high ductility engineered cementitious composites as a novel and resilient fireproof coating. *Constr. Build. Mater.* 288, 123090. doi:10.1016/j.conbuildmat.2021.123090

Ding, Y., Yu, K. Q., and Li, M. (2021). A review on high-strength engineered cementitious composites (HS-ECC): Design, mechanical property and structural application. *Structures* 35, 903–921. doi:10.1016/j.istruc.2021.10.036

Ekmekyapar, T., and Alhatmey, I. A. H. (2019). Post-fire resistance of internally ring stiffened high performance concrete filled steel tube columns. *Eng. Struct.* 183, 375–388. doi:10.1016/j.engstruct.2019.01.024

Ghorbi, E., Soltania, M., and Maekawab, K. (2013). Development of a compressive constitutive model for FRP-confined concrete elements. *Composite: Part B* 45, 504–517. doi:10.1016/j.compositesb.2012.07.014

Gu, W. P., Cai, S. H., and Feng, W. L. (1991). Behavior and ultimate strength of steel tubes filled with high strength concrete. *Build. Sci.* 1, 23–27. doi:10.13614/j.cnki.11-1962/tu.1991.01.005

Guler, S., Çopur, A., and Aydogan, M. (2013). Axial capacity and ductility of circular uhpc-filled steel tube columns. *Mag. Concr. Res.* 65, 898–905. doi:10.1680/macr.12.00211

Han, L. H. (2007). *Concrete filled steel tube structures: Theory and practice.* Beijing: Science Press.

Han, L. H., and Yao, G. H. (2004). Experimental behaviour of thin-walled hollow structural steel (HSS) columns filled with self-consolidating concrete (SCC). *Thin-walled Struct.* 42, 1357–1377. doi:10.1016/j.tws.2004.03.016

Ho, J. C. M., Lai, M. H., and Luo, L. (2013). Uniaxial behaviour of confined high-strength concrete-filled-steel-tube columns. *Proc. Institution Civ. Eng. - Struct. Build.* 167, 520–533. doi:10.1680/stbu.13.00004

Huang, C. K., Shang, Z. Q., and Zhang, P. (2009). Experimental research on self-stressing and self-compacting concrete-filled steel tube columns subjected to eccentric load. *Front. Archit. Civ. Eng. China* 3. *RESEARCH ARTICLE.* 2009-09-23. doi:10.1007/s11709-009-0058-6

Ji, J., He, L. J., Jiang, L. Q., Ren, H, Ni, S, Wang, Z, et al. (2021b). Seismic behavior of GFRP tube reactive powder concrete composite columns with encased steel. *Front. Mater.* 8, 793392. doi:10.3389/fmats.2021.793392

Ji, J., Kang, W., Jiang, L. Q., Li, Y, Ren, H, Hao, S, et al. (2021c). Mechanical behavior of reactive powder concrete made from local material subjected to axial pressure. *Front. Mater.* 8, 737646. doi:10.3389/fmats.2021.737646

Ji, J., Yu, C. Y., Jiang, L. Q., Zhan, J, Ren, H, Hao, S, et al. (2022). Bearing behavior of H-shaped honeycombed steel web composite columns with rectangular concrete-filled steel tube flanges under eccentrical compression load. *Adv. Civ. Eng.* 2022, 2965131. doi:10.1155/2022/2965131

Ji, J., Yu, D. Y., Jiang, L. Q., Liu, Y. C., Yang, M. M., Song, H. Y., et al. (2020). Research on axial compression bearing capacity of different-strength concrete-filled double steel tube stub columns. *Build. Struct.* 50 (5), 120–129. doi:10.19701/jjzjg2020.05.021

Ji, J., Zeng, W., Jiang, L. Q., Bai, W, Ren, H, Chai, Q, et al. (2021a). Hysteretic behavior on asymmetrical composite joints with concrete-filled steel tube columns and unequal high steel beams. *Symmetry* 13 (12), 2381. doi:10.3390/sym13122381

Ji, J., Zeng, W., Wang, R. L., Ren, H, Zhang, L, Liu, Y, et al. (2021d). Bearing capacity of hollow FRP tube-concrete-high strength steel tube composite long columns under eccentric compression load. *Front. Material* 9, 27. doi:10.3389/fmats.2021.768877

Lee, H. J., Parka, H. G., and Choi, I. R. (2019). Eccentric compression behavior of concrete-encased-and-filled steel tube columns with high-strength circular steel tube. *Thin-Walled Struct.* 144, 106339. doi:10.1016/j.tws.2019.106339

Li, G. C., Liu, D., Yang, Z. J., and Zhang, C. Y. (2019). Flexural behavior of high strength concrete filled high strength square steel tube. *J. Constr. Steel Res.* 128, 732–744. doi:10.1016/j.jcsr.2016.10.007

Luo, X., Wei, J. G., Han, J. P., and Chen, B. C. (2021). Experimental study on compression performance of ultra-high-strength concrete (UHSC) filled high-strength steel tube stub columns subjected to eccentric load. *J. Build. Struct* 42 (Suppl. 2), 271–277. doi:10.14006/j.jzjgxb2021.S2.0032

Mander, J. B., Priestley, M. J. N., and Park, R. (1988). Theoretical stress-strain model for confined concrete. *J. Struct. Eng.* 114 (8), 1804–1826. doi:10.1061/(asce)0733-9445(1988)114:8(1804)

Mao, M, Tong, K. T., Zhang, J. L., Liu, T., and Li, Y. (2021). Experimental study on the mechanical performance of steel-bamboo composite I-section columns under eccentric loading. *J. Build. Struct.* 42 (8), 126–135. doi:10.4006/j.jzjgxb.2019.0414

Pagoulatou, M., Sheehan, T., Dai, X. H., and Lam, D. (2014). Finite element analysis on the capacity of circular concrete-filled double-skin steel tubular

(CFDST) stub columns. *Eng. Struct.* 72, 102–112. doi:10.1016/j.engstruct.2014.04.039

Qian, J. R., Chen, L. R., and Zhou, D. L. (2002). Central compression behavior of concrete columns confined by ordinary stirrups. *Tsinghua Sci. Technol.* 42 (10), 1369–1373. doi:10.16511/j.cnki.qhdxxb.2002.10.024

Sung, W. Y., Seung-Jun, K., and Jung, S. H. (2012). Analysis technique for autogenous shrinkage in high performance concrete with mineral and chemical admixtures. *Constr. Build. Mater.* 34, 1–10. doi:10.1016/j.conbuildmat.2012.02.005

Tao, Z., Wang, Z. B., and Yu, Q. (2013). Finite element modelling of concrete-filled steel stub columns under axial compression. *J. Constr. Steel Res.* 89, 121–131. doi:10.1016/j.jcsr.2013.07.001

Teng, J. G., Yu, T., Wong, Y. L., and Dong, S. (2006). Hybrid FRP–concrete–steel tubular columns: Concept and behavior. *Constr. Build. Mat.* 21 (4), 846–854. doi:10.1016/j.conbuildmat.2006.06.017

Wang, F. C., Zhao, H. Y., and Han, L. H. (2019). Analytical behavior of concrete-filled aluminum tubular stub columns under axial compression. *Thin-Walled Struct.* 140 (30), 21–30. doi:10.1016/j.tws.2019.03.019

Wang, Q. L., Hou, T. T., Li, Q. G., and Wang, Y. (2013). Static performance of the high-performance concrete filled steel tube stub column (1): Experimental study and fine element simulation. *Ind. Constr.* 43 (3), 24–29. doi:10.13204/j.gyjz201303005

Wang, Z. J., and Liang, J. B. (2012). Research and applying evolution of admixture for high-performance concrete. *Appl. Mech. Mater.* 2012 (174-177), 1086–1189. doi:10.4028/AMM

Wei, J. G., Luo, X., Ou, Z. J., and Chen, B. (2019). Experiment study on axial compressive behavior of circular UHPC filled high-strength tube stub columns. *J. Build. Strustures* 41, 16–28. doi:10.14006/j.jzjgxb.2019.0337

Yang, Y. B., Liang, S., Mo, H. H., Chen, Y. W., Chen, J. S., and Ba, L. Z. (2009). Research on high-performance concrete-filled steel tube columns structure experiments of guangzhou xita Project. *Key Eng. Mater.* 405-406, 50–54. doi:10.4028/www.scientific.net/KEM.405-406.50-40

Yoo, S. W., Kwon, S. J., and Jung, S. H. (2012). Analysis technique for autogenous shrinkage in high-performance concrete with mineral and chemical admixtures. *Constr. Build. Mater.* 34 (12), 1–10. doi:10.1016/j.conbuildmat.2012.02.005

Yoon, Y. S., and Jang, I. Y. (2015). Effects of quality of compaction on flexural behaviour of high-performance concrete beams. *Mag. Concr. Res.* 54 (4), 283–290. doi:10.1680/macr.54.4.283.38804

Yu, Q., Tao, Z., and Wu, Y. X. (2009). Behavior of high-performance concrete-filled steel tube columns subjected to eccentric loading. *Eng. Mech.* 26 (10), 87–094.

Yu, Q., Tao, Z., and Wu, Y. X. (2007). Experimental behaviour of high performance concrete-filled steel tubular columns. *Thin-Walled Struct.* 2008-46 (4), 362–370. doi:10.1016/j.tws.2007.10.001

Yu, Z. W., Ding, F. X., and Lin, S. (2002). Researches on behavior of high-performance concrete-filed steel tube stub columns. *J. Build. Struct.* 23 (2), 41–47. doi:10.14006/j.jzjgxb.2002.02.006

Zhu, M. C., Liu, J. X., Wang, Q. X., and Feng, X. F. (2010). Experimental research on square steel tubular columns filled with steel-reinforced self-consolidating high-strength concrete under axial load. *Eng. Struct.* 32, 2278–2286. doi:10.1016/j.engstruct.2010.04.002